2013 IEEE International Conference on Robotics and Automation (ICRA)
Karlsruhe, Germany, May 6-10, 2013

A Flapping-Wing Microrobot with a Differential Angle-of-Attack Mechanism

Z. E. Teoh and R. J. Wood

Abstract— **Control of insect-scale flapping-wing robots is challenging due to weight constraints and inherent instabilities. Instead of adding more actuators to increase the controllability of the flapping-wing robot, we use a single actuator to drive a system of mechanical linkages to cause bilaterally asymmetric changes in the wing hinge spring rest angle of the left and right wings. We show in simulation that such a control input can generate wing motions which produce yaw and roll torques. A kinematic model of the mechanism was developed and an at-scale prototype of this concept was built. High speed videos of its wing motions are consistent with the kinematic model and according to the simulation, are capable of generating adequate yaw and roll torques for attitude control.**

I. Introduction

The agility of hummingbirds, dragonflies, bees, and fruit flies has inspired scientist to study how they use flapping wings as a means to generate aerodynamic forces capable of producing often complex maneuvers in air. Various groups have reported success in building Micro Air Vehicles (MAV) using rotary-motors to drive flapping wings and propellors, rubber bands to power butterfly-like wings and rotary motions that mimic the flight of samara seeds [1], [2], [3], [4]. As we try to shrink the MAV to insect-scale, use of conventional components such as rotary motors, bearings and airfoils become inefficient. This is due to dominating effects of surface and viscous forces over Newtonian forces [5] and lift producing aerodynamic inertial forces respectively.

To design a flapping-wing microrobot to work in such a different environment, our group takes inspiration from bees and flies, constructing our MAV (termed the RoboBee) from components that have an analog to features normally associated with bees (and other flying insects which use asynchronous muscles [6]). The flight muscle of the RoboBee is a piezoelectric bimorph actuator that converts a linear input to an angular output which drives a pair of wings through a transmission (thorax). By harnessing passive wing rotation (a phenomenon also observed in nature [7]), the Harvard Microrobotic Fly (HMF) [8] was the first insect-scale robot to achieve a thrust-to-weight ratio greater than one. To control more degrees-of-freedom, small piezoelectric bimorph control actuators were added within the thorax of the RoboBee, enabling the wings to have different stroke amplitudes [9]. Finio's design of the RoboBee produced roll torques by applying static control inputs and yaw torques by phasing the control input with respect to the power input. A hybrid approach taken by Ma et al.– using two piezoelectric bimorph actuators to drive each wing independently– showed that it could generate sufficient torques for control purposes [10]. Ma's design generated roll torques by independently increasing/decreasing the stroke amplitude of a wing and created yaw torques by adjusting the upstroke and downstroke velocities of its power actuators. All previous designs can generate pitch torques by biasing the power actuator forward or backward (this gives the direction of the pitch torque). An alternative way to generate torques for control is by varying the Angle-of-Attack (AoA) of the wings.

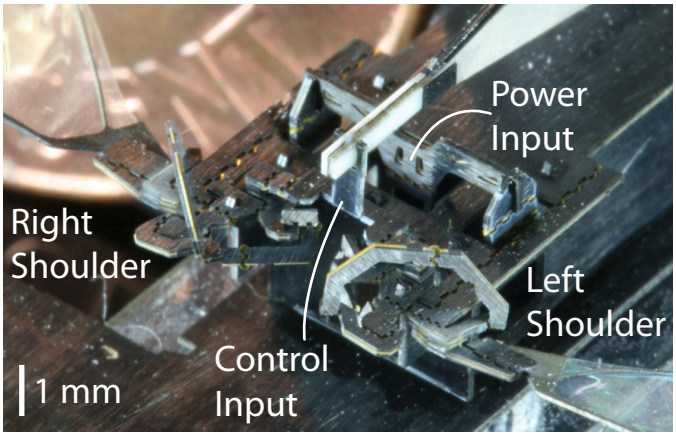

Fig. 1. Prototype of the RoboBee. The control actuator is shown here located dorsally while the power actuator is hidden ventrally by the support structure. A U.S. penny in the background is shown for scale.

If the AoA of each wing can be tuned to achieve different lift and drag force profiles, control torques can be generated [11]. By measuring the untethered flight kinematics of fruit flies, Bergou et al. modeled a fly's wing hinge as a torsional spring that passively opposes the wing's tendency to over rotate due to aerodynamic and inertial forces. By changing the spring rest angle, an asymmetric AoA can be generated in the upstroke and downstroke of the fly [12]. In this paper we report progress in changing the AoA of the RoboBee's wings by using a system of mechanical linkages to cause bilaterally asymmetric changes to the wing hinge spring rest

This work was partially supported by the National Science Foundation (award numbers CCF-0926148 and CMMI-0746638) and the Wyss Institute for Biologically Inspired Engineering. Any opinions, findings, and conclusions or recommendations expressed in this material are those of the authors and do not necessarily reflect the views of the National Science Foundation.

The authors are with the School of Engineering and Applied Sciences, Harvard University, Cambridge MA 02138 USA and the Wyss Institute for Biologically Inspired Engineering, Harvard University, Boston, MA 02115, USA(E-mail: zhiernteoh@seas.harvard.edu and rjwood@eecs.harvard.edu)

U.S. Government work not protected by U.S. copyright

TABLE I
NOTATION

Symbol(s)	Meaning
${}^{A}R^{B} \equiv R_{\hat{b_k}}(D)$	Rotation matrix mapping the right-handed orthogonal unit vectors $\hat{b}_x$, $\hat{b}_y$ and $\hat{b}_z$ to the right-handed orthogonal unit vectors $\hat{a}_x$, $\hat{a}_y$ and $\hat{a}_z$ via a positive rotation of angle D about $\hat{b}_k$ where k=x,y or z
$\vec{r}^{\,E/F}$	Position vector of point E from F
$\vec{g} \cdot \vec{f}$	dot product of vector $\vec{g}$ and $\vec{f}$
$\hat{h}$	a unit vector
s_θ	$sin(\theta)$
c_θ	$cos(\theta)$
t_θ	$tangent(\theta)$

angle by using a single control actuator. We simulate the effect of changing the wing hinge spring rest angle on the aerodynamic force produced by each wing—showing that yaw torques can be created by biasing the control actuator and roll torques are produced by phasing the control actuator with respect to the power actuator (this concept flips the way yaw and roll torque is generated as compared to [9]). We construct a kinematic model of the mechanism and build an at-scale non-flight weight RoboBee to verify that we can generate wing motions as predicted by the kinematic model.

II. MECHANICAL DESIGN AND KINEMATIC MODEL

Power to the RoboBee is provided by a single piezoelectric bimorph actuator in a configuration similar to the design in [13]. The power actuator provides a linear input $\delta_{P_{I_z}}$ to two planar four-bar linkages which results in angular outputs ϕ_J, where J=Left (L) or Right (R), are defined to be the RoboBee's left and right stroke amplitudes respectively (Tables I and II detail the notation and variables used in this paper. See table III for rotation matrix definitions that relate the rotation of a rigid link with respect to its neighboring rigid links in Fig. 2 [14]).

To combine the power and control inputs in a decoupled manner, the Sreetharan linkage [15], a spherical five-bar linkage, was used to combine an angular control input $\psi_{0J,i}$ along $\hat{n_y}$ and an angular power input ϕ_J along $\hat{n_x}$. Instead of using two control actuators [9], the left and right side of the RoboBee are coupled differentially by two planar four-bar linkages driven by a single piezoelectric bimorph control actuator.

The control input mechanism consists of two planar four-bar linkages connected in series. When a positive control input $\delta_{C_{I_y}}$ is applied at C_I, C_{RA} deflects downward in the $\hat{n}_z$ direction while C_{LA} deflects upward in the $-\hat{n}_z$ direction (See Fig. 2). This causes the left and right sides of the RoboBee to have differential angular outputs ψ_{oJ} at the wing hinge connectors S_{L3} and S_{R3} respectively (Fig. 2C).

The long axis of the control actuator is designed to be mounted along $\hat{n_x}$ to minimize the weight of the overall support structure by using the same support structure holding the power actuator. This caused the quasi-linear control input to be applied in the $\hat{n_y}$ direction which translates into angular inputs around the $\hat{n_x}$ axis. Since the Sreetharan linkage was designed to take in the angular control input along the $\hat{n_y}$ axis, a spherical four-bar linkage was used to rotate the control input $\theta_{C_{JA}}$from along $\hat{n_x}$ to $\hat{n_y}$ about $\hat{n_z}$ to the wing hinge spring rest angle input $\psi_{0J,i}$ (Fig. 2B). The power angular input (ϕ_J) is conveniently located along the required $\hat{n_x}$ direction which enables it to couple directly to the Sreetharan linkage (Fig. 2B).

In order to construct the kinematics of the device, position constraints are applied to close the kinematic chains. Starting from the left side of the RoboBee with the control input (Fig. 2C), the position of $c_{LB}c_I$ is constrained according to:

$$\vec{r}^{\,c_{LB}c_I/N_o} \cdot \hat{n}_z = -L_3 \tag{1}$$

$$\vec{r}^{\,c_{LB}c_I/N_o} \cdot \hat{n}_y - \delta_{C_{I_y}} = L_1 + L_2 - L_4. \tag{2}$$

Moving along the chain, the four-bar spherical linkage (Fig. 2B) is knitted together by the joint connecting S_{L1} and D_L:

$$\hat{s}_{L1',z} \cdot \hat{d}_{L,z} = 1 \tag{3}$$

$$\hat{s}_{L1',z} \cdot \hat{d}_{L,x} = 0. \tag{4}$$

Next to the four-bar spherical linkage (Fig. 2B), the Sreetharan linkage is constrained by the joint connecting S_{L3} and S_{L2}:

$$\hat{s}_{L3,z} \cdot \hat{s}_{L2,z} = 1 \tag{5}$$

$$\hat{s}_{L3,z} \cdot \hat{s}_{L2,x} = 0. \tag{6}$$

Finally, ending at the power input of the left side of the RoboBee, the position of $p_{LB}p_I$ is constrained according to:

$$\vec{r}^{\,p_{LB}p_I/N_o} \cdot \hat{n}_y = L_3 \tag{7}$$

$$\vec{r}^{\,p_{LB}p_I/N_o} \cdot \hat{n}_z - \delta_{P_{I_z}} = -L_1 - L_2 + L_4. \tag{8}$$

By repeating the constraints on the right side of the RoboBee, eight more constraints are formed. The resulting sixteen constraints form a nonlinear system of equations with the following unknowns:

$$\vec{x}_L = \left[\ \theta_{C_{LA}} \quad \theta_{C_{LB}} \quad \beta_L \quad \psi_{oL,i} \quad \gamma_L \quad \psi_{oL} \quad \phi_L \quad \theta_{P_{LB}}\ \right]$$
$$\vec{x}_R = \left[\ \theta_{C_{RB}} \quad \theta_{C_{RA}} \quad \beta_R \quad \psi_{oR,i} \quad \gamma_R \quad \psi_{oR} \quad \phi_R \quad \theta_{P_{RB}}\ \right],$$
$$\vec{x} = [\vec{x}_L, \vec{x}_R], \tag{9}$$

and $\delta_{C_{I_y}}$, $\delta_{P_{I_z}}$ the inputs to the system. These equations can be expressed as follows:

$$f_i(\vec{x}, \delta_{C_{I_y}}, \delta_{P_{I_z}}) = 0, i = 1 \ldots 16. \tag{10}$$

By differentiating the position constraints to form velocity constraints:

$$g_i(\dot{\vec{x}}, \vec{x}, \dot{\delta}_{C_{I_y}}, \dot{\delta}_{P_{I_z}}) = 0, \tag{11}$$

the resulting system of equations is linear with respect to $\dot{\vec{x}}$

$$\dot{\vec{x}} = h_i(\vec{x}, \dot{\delta}_{C_{I_y}}, \dot{\delta}_{P_{I_z}}), i = 1 \ldots 16\,. \tag{12}$$

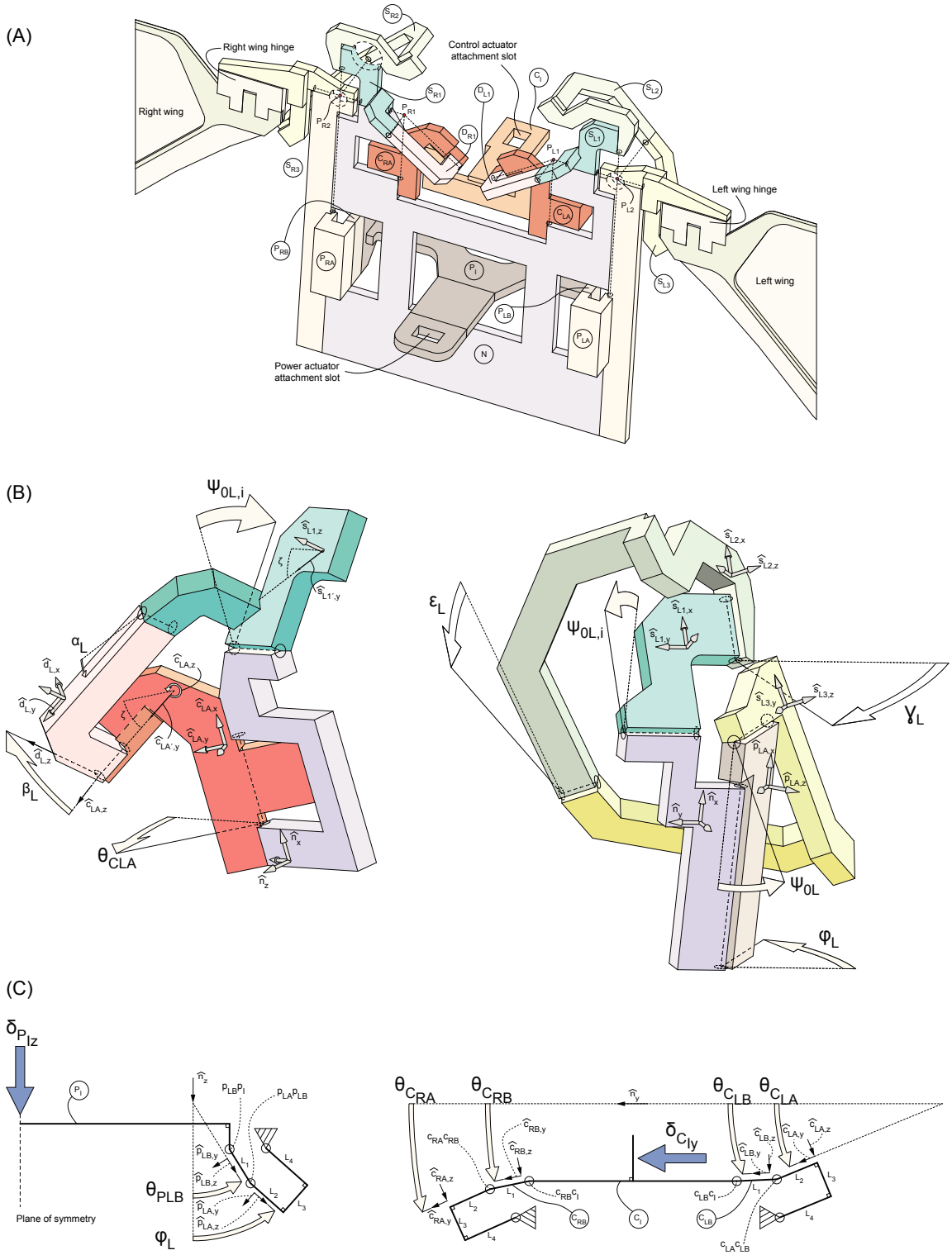

Fig. 2. (A) Overview of the proposed mechanism that enables the left and right wings to have different wing hinge rest angle. (B) Shown here are the spherical linkages on the left side of the RoboBee. From the left to the right of the page, a spherical four-bar linkage rotates the rotation axis of an angular input by 90° and a Sreetharan linkage (spherical five-bar linkage) that combines two independent angular inputs and maps them onto the wing hinge connector S_{L3}. The centers of the linkages are shown as solid red circles in (A) are P_{L1} and P_{L2} respectively. We define such a combination of linkages as the left shoulder of the RoboBee (C) The power actuator is connected to two planar four-bar linkages (only one is shown here due to symmetry) while the control actuator is connected to another two planar four-bar linkages that produces differential angular input angles to the spherical four-bar linkages.

TABLE II

LIST OF VARIABLES AND THEIR DEFINITIONS

Quantity	Identifier	Type	Initial Value (for variables)
Distance between $p_{JB}p_I/c_{JB}c_I$ and $p_{JA}p_{JB}/c_{JA}c_{JB}$	L_1	constant	0.44 mm
Length of a link in P_{JA}/C_{JA}	L_2	constant	0.48 mm
Length of a link in P_{JA}/C_{JA}	L_3	constant	0.40 mm
Length of a link in P_{JA}/C_{JA}	L_4	constant	0.61 mm
Control input from C_I to the control transmission	$\delta_{C_{I_y}}$	specified	
Power input from P_I to the power transmission	$\delta_{P_{I_z}}$	specified	
Angle between $\hat{n}_y$ and $\hat{c}_{JA,y}$	$\theta_{C_{JA}}$	variable	0°
Angle between $\hat{n}_y$ and $\hat{c}_{JB,y}$	$\theta_{C_{JB}}$	variable	0°
Angle between $\hat{n}_z$ and $\hat{p}_{JA,z}$	ϕ_J	variable	0°
Angle between $\hat{n}_z$ and $\hat{p}_{JB,z}$	$\theta_{P_{JB}}$	variable	0°
Angle between $\hat{c}_{JA,z}$ and $\hat{d}_{J,z}$	β_J	variable	0°
Angle between $\hat{s}_{J1',y}$ and $\hat{d}_{J,y}$	α_J	variable	0°
Angle between $\hat{s}_{L1,y}$ and $\hat{s}_{L1',y}$	ζ	constant	35°
Angle between $\hat{c}_{LA,y}$ and $\hat{c}_{LA',y}$	ζ	constant	35°
Angle between $\hat{s}_{R1,y}$ and $\hat{s}_{R1',y}$	$-\zeta$	constant	-35°
Angle between $\hat{c}_{RA,y}$ and $\hat{c}_{RA',y}$	$-\zeta$	constant	-35°
Angle between $\hat{n}_x$ and $\hat{s}_{J1,x}$	$\psi_{0J,i}$	variable	0°
Angle between $\hat{s}_{J1,y}$ and $\hat{s}_{J2,y}$	γ_J	variable	0°
Angle between $\hat{s}_{J2,x}$ and $\hat{s}_{J3,x}$	ϵ_J	variable	0°
Angle between $\hat{p}_{JA,x}$ and $\hat{s}_{J3,x}$	ψ_{0J}	variable	0°

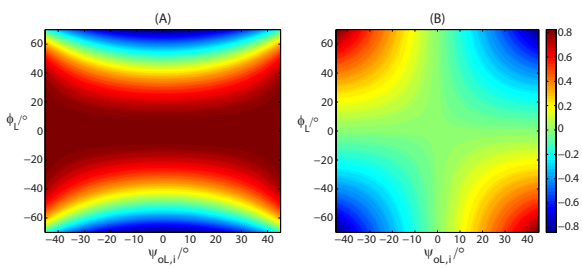

Fig. 3. (A) Contour map of $\frac{\partial \psi_{oL}}{\partial \psi_{oL,i}}$ (B) Contour map of $\frac{\partial \psi_{oL}}{\partial \phi_L}$

Given the initial conditions $\vec{x}_0$, a specified $\dot{\delta}_{C_{I_y}}$ and $\dot{\delta}_{P_{I_z}}$, the kinematics of the RoboBee are found by stepping forward in time.

A. Transmission Characteristics

1) Spherical Four-bar Linkage: Picking the left side of the RoboBee, we expand both eqn. (3)

$$1 = c_{\beta_L} c_{\theta_{C_{LA}}} c_{\psi_{oL,i}} + s_{\beta_L}(c_\zeta s_{\psi_{oL,i}} + s_\zeta s_{\theta_{C_{LA}}} c_{\psi_{oL,i}})$$

to form

$$\frac{1}{c_{\beta_L} c_{\theta_{C_{LA}}} c_{\psi_{oL,i}}} = 1 + \frac{s_{\beta_L}(c_\zeta s_{\psi_{oL,i}} + s_\zeta s_{\theta_{C_{LA}}} c_{\psi_{oL,i}})}{c_{\beta_L} c_{\theta_{C_{LA}}} c_{\psi_{oL,i}}} \tag{13}$$

and eqn. (4)

TABLE III

DEFINITION OF ROTATION MATRICES USED IN THE KINEMATIC MODEL

Power Transmission	${}^{P_{JA}}R^N \equiv R_{\hat{n}_x}(\phi_J)$
	${}^{P_{JB}}R^N \equiv R_{\hat{n}_x}(\theta_{P_{JB}})$
Control Transmission	${}^{C_{JA}}R^N \equiv R_{\hat{n}_x}(\theta_{C_{JA}})$
	${}^{C_{JB}}R^N \equiv R_{\hat{n}_x}(\theta_{C_{JB}})$
Spherical Four-bar Linkage	${}^{C_{JA}}R^N \equiv R_{\hat{n}_x}(\theta_{C_{JA}})$
	${}^{C_{JA'}}R^{C_{JA}} \equiv \begin{cases} R_{\hat{c}_{LA,z}}(\zeta) \\ R_{\hat{c}_{RA,z}}(-\zeta) \end{cases}$
	${}^{S_{J1'}}R^{S_{J1}} \equiv \begin{cases} R_{\hat{s}_{J1,z}}(\zeta) \\ R_{\hat{s}_{R1,z}}(-\zeta) \end{cases}$
	${}^{D_J}R^{C_{JA'}} \equiv R_{\hat{c}_{JA',y}}(\beta_J)$
	${}^{S_{J1}}R^N \equiv R_{\hat{n}_y}(\psi_{0J,i})$
Sreetharan Linkage	${}^{P_{JA}}R^N \equiv R_{\hat{n}_x}(\phi_J)$
	${}^{S_{J3}}R^{P_{JA}} \equiv R_{\hat{p}_{JA,y}}(\psi_{0J})$
	${}^{S_{J1}}R^N \equiv R_{\hat{n}_y}(\psi_{0J,i})$
	${}^{S_{J2}}R^{S_{J1}} \equiv R_{\hat{s}_{J1,x}}(\gamma_J)$

$$0 = c_{\beta_L}(c_\zeta s_{\psi_{oL,i}} + s_\zeta s_{\theta_{C_{LA}}} c_{\psi_{oL,i}}) - s_{\beta_L} c_{\theta_{C_{LA}}} c_{\psi_{oL,i}}$$

to form

$$\frac{s_{\beta_L}}{c_{\beta_L}} = \frac{c_\zeta s_{\psi_{oL,i}} + s_\zeta s_{\theta_{C_{LA}}} c_{\psi_{oL,i}}}{c_{\theta_{C_{LA}}} c_{\psi_{oL,i}}}. \tag{14}$$

By substituting eqn. (14) into eqn. (13) we get,

$$c_{\beta_L} = c_{\theta_{C_{LA}}} c_{\psi_{oL,i}}. \tag{15}$$

Using small angle approximations to eqn. (14) and eqn. (15) results in,

$$\beta_L = c_\zeta \psi_{oL,i} + s_\zeta \theta_{C_{LA}} \tag{16}$$

$$\beta_L^2 = \psi_{oL,i}^2 + \theta_{C_{LA}}^2 - \frac{\psi_{oL,i}^2 \theta_{C_{LA}}^2}{2}. \tag{17}$$

After combining eqn. (16) and eqn. (17), the resulting higher order terms are removed which yields the following relation between the input $\theta_{C_{LA}}$ and the output $\psi_{0L,i}$:

$$\psi_{oL,i} = \left(\frac{1}{t_\zeta}\right)\theta_{C_{LA}}. \tag{18}$$

This enables us to pick values of ζ to amplify or reduce the output of the linkage. Here, our goal is to rotate the input and keep the magnitude the same. We chose $\zeta = 35°$ because our simulations indicated that $\psi_{oL,i} \approx \theta_{C_{LA}}$ over a larger range of input angles as compared to a linkage with $\zeta = 45°$ where at larger input angles $\psi_{oL,i} < \theta_{C_{LA}}$.

2) Sreetharan Linkage: By expanding eqn. (6) we have,

$$0 = s_{\psi_{oL}} c_{\psi_{oL,i}} - s_{\psi_{oL,i}} c_{\psi_{oL}} c_{\phi_L} \tag{19}$$

After simplification, this yields the following relationship:

$$t_{\psi_{oL}} = t_{\psi_{oL,i}} c_{\phi_L} \tag{20}$$

To examine how the coupling of the inputs $\psi_{oL,i}$ and ϕ_L affects the left wing spring rest angle, ψ_{oL}, the partial

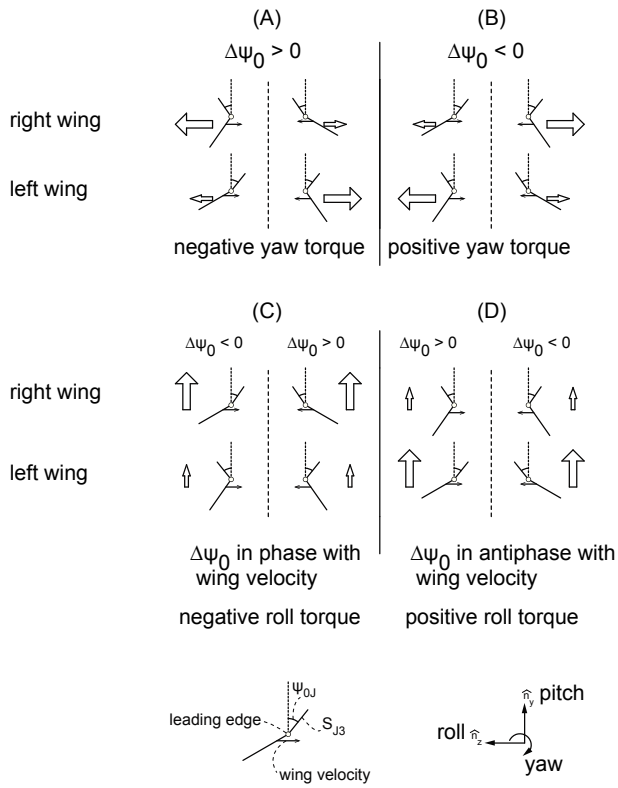

Fig. 4. Yaw and roll torques can be generated by modulating the DC value, B, and the phase, Φ, of $\triangle\psi_0$.

derivative of ψ_{oL} with respect to its inputs are calculated. The partial derivatives are plotted in Fig. 3 where ϕ_L and $\psi_{oL,i}$ are limited to the domains $[-70°, 70°]$ and $[-45°, 45°]$ respectively. $\frac{\partial\psi_{oL}}{\partial\psi_{oL,i}} \approx 1$ and $\frac{\partial\psi_{oL}}{\partial\phi_L} \approx 0$ over a wide range of the input parameter space which indicates that the control input $\psi_{oL,i}$ maps to ψ_{oL} well and is largely decoupled from the power input ϕ_L.

$$\frac{\partial\psi_{oL}}{\partial\psi_{oL,i}} = \frac{c_{\phi_L}}{c^2_{\psi_{oL,i}}[1 + (t_{\psi_{oL,i}} c_{\phi_L})^2]} \tag{21}$$

$$\frac{\partial\psi_{oL}}{\partial\phi_L} = \frac{-s_{\phi_L} t_{\psi_{oL,i}}}{[1 + (t_{\psi_{oL,i}} c_{\phi_L})^2]} \tag{22}$$

III. Generating Yaw and Roll Torques

Pitch torques have been shown in [9] to be generated by biasing the offset voltage of the power actuator. Since, for the case of $\delta_{C_{I_y}} = 0$ (i.e. zero control actuator motion) this design is identical to that in [9], pitch torques are created in the same manner. Here, we provide an alternative way of generating yaw and roll torques by causing bilaterally asymmetric changes to the wing hinge spring rest angles, ψ_{0J}, of the RoboBee.

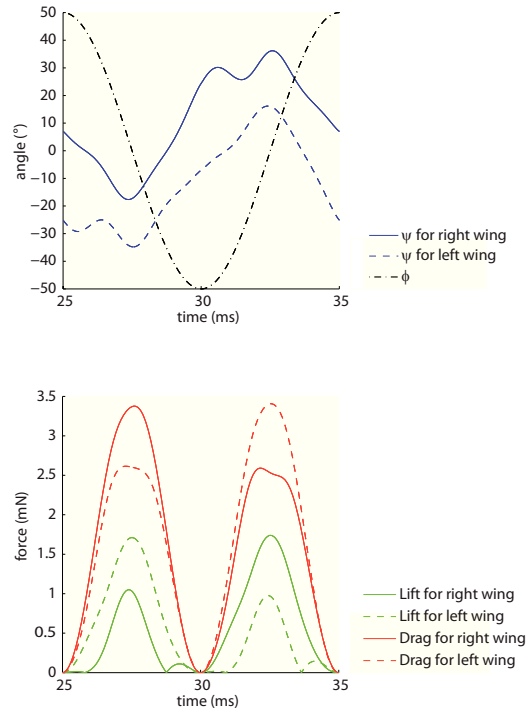

Fig. 5. Simulation of ψ and ϕ with $\triangle\psi_0 = \frac{\pi}{6}$ and wing hinge stiffness of 5.5 $\frac{\mu Nm}{rad}$. Here the asymmetric drag profiles on the left and right wing generate a mean yaw torque of 4 μNm.

For small inputs into the system, we can simplify the kinematics greatly to gain insight into how the control actuator input will affect ψ_{0J}. Applying small angle approximations to eqn. (2) gives

$$\theta_{C_{JA}} = \frac{1}{L_3}\delta_{C_{I_y}} \tag{23}$$

Similarly, eqns. (18) and (20) reduce to

$$\psi_{oJ,i} = \begin{cases} \left(\frac{1}{t_\zeta}\right)\theta_{C_{LA}} \\ -\left(\frac{1}{t_\zeta}\right)\theta_{C_{RA}} \end{cases} \tag{24}$$

$$\psi_{0J} = \psi_{0J,i} \tag{25}$$

Defining the relative difference between the left and right wing hinge spring rest angles as,

$$\triangle\psi_0 \equiv \psi_{0L} - \psi_{0R}, \tag{26}$$

and combining eqns. (23) to (25), an expression relating $\delta_{C_{I_y}}$ to $\triangle\psi_0$ is found to be,

$$\triangle\psi_0 = \frac{2}{t_\zeta L_3}\delta_{C_{I_y}} \tag{27}$$

Based on kinematic data from fruit flies ($D.melanoaster$), Bergou, et al. proposed that the flies use a non-zero $\triangle\psi_0$ to generate yaw torques by creating asymmetries in the AoA of the downstroke and upstroke [12]. Work by Mahjoubi and Byl showed that a constant non-zero ψ_{0j} can produce asymmetric lift on the upstroke and downstroke (whether more lift occurs on the upstroke or downstroke depends on the sign of ψ_{0j}) [11].

In order to generate roll torques, we would need to generate more lift on both the downstroke and upstroke strokes of either wing (this implies the other wing would have less lift due to coupling of the left and right sides of the RoboBee). This is done by driving the control actuator at the same frequency as the power actuator and in phase or anti-phase with $\dot{\phi}$. Using the blade element method [16] to simulate the effect of ψ_{0j} on the aerodynamic forces produced by the wings, we show in Fig. 5 and 6 that it is possible to generate yaw and roll torques by modulating the DC value and phase of $\triangle\psi_0$ (ψ the pitch of the wing is defined in [16]).

In this simulation, only one wing is driven. We can simulate the effect of two wings and the control mechanism by simulating the left and right wing independently by prescribing a wing stroke function:

$$\phi_J = -A_\phi cos(2\pi ft), \tag{28}$$

and a wing hinge spring rest angle input function, one for the left and another for the right hinge:

$$\psi_{0L} = A_\psi sin(2\pi ft + \Phi) + B \tag{29}$$

$$\psi_{0R} = A_\psi sin(2\pi ft + \Phi - \pi) - B \tag{30}$$

which is equivalent to an input of

$$\triangle\psi_0 = 2A_\psi sin(2\pi ft + \Phi) + 2B, \tag{31}$$

where A_ϕ is half the peak-to-peak value of ϕ_J, A_ψ is half the peak-to-peak value of ψ_{0J}, f the flapping frequency of the wing and B the DC value. Φ, the phase of the wing hinge spring rest angle, is π or 0 depending on the desired roll torque direction. To simulate a yaw maneuver (Fig. 4A), we set $A_\phi = 50°$, $f = 100$ Hz $A_\psi = 0°$, $B = 15°$ and $\Phi = 0°$. The resulting aerodynamic force profile (Fig. 5) generates a mean yaw torque of 4 μNm and a mean lift of 1.06 mN. Next, a roll maneuver (Fig. 4C) was simulated by setting $A_\phi = 50°$, $f = 100$ Hz $A_\psi = 15°$, $B = 0°$ and $\Phi = 0°$ which generates a mean roll torque of 3.7 μNm with a mean lift of 1.16 mN (Fig. 6).

IV. Experiments and Results

The kinematic model presented is a useful tool to guide the design of the RoboBee. In order to validate the model, an at-scale non-flight weight version was built. The kinematic model assumes that the linkages are rigid, the joints are revolute with flexures acting as torsional springs and perfectly aligned 90° folds. In practice, these assumptions are extremely difficult to achieve. By using techniques from [17], we can, to a certain degree, approach the kinematic alignment necessary for such a device to function. However, for this prototype, simple manual folding with kinematic stops were used to align 90° folds. This fabrication technique, though not as precise, was less complex in its design which suited our goal of creating the first prototype of this RoboBee concept.

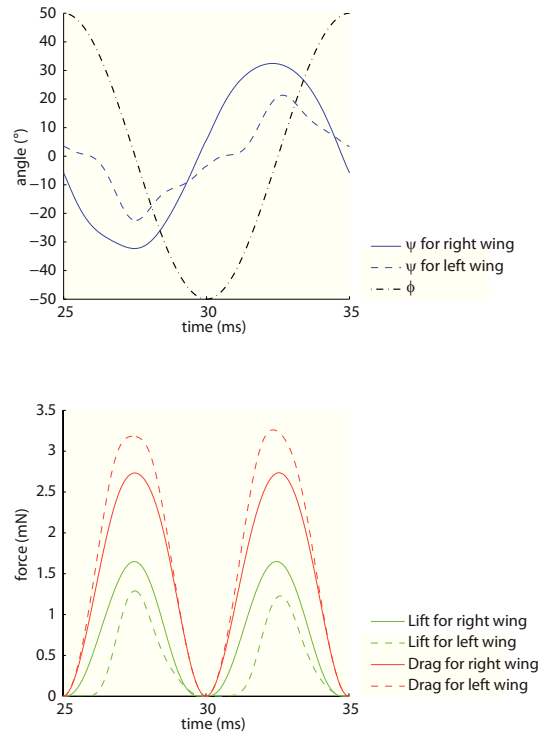

Fig. 6. Simulation of ψ and ϕ with $\triangle\psi_0 = \frac{\pi}{6} sin\,(2\pi t)$ and wing hinge stiffness of 5.5 $\frac{\mu Nm}{rad}$. Here the asymmetric lift profiles on the left and right wing generate a mean roll torque of 3.7 μNm.

The piezoelectric bimorph actuator [18] is made from two Lead Zirconate Titanate (PZT) plates (Piezo Systems Inc.) sandwiching a carbon layer. A bias voltage of 300V is applied to the top plate and 0V applied to the bottom plate (order depends on poling direction of the PZT plate). The control signal is

$$V_{carbon} = \frac{A_{peak-to-peak}}{2} sin(2\pi ft + \Phi_{signal}) + V_{offset}$$

applied at the carbon layer which induces a quasi-linear deflection at the tip of the actuator. $A_{peak-to-peak}$ is the peak-to-peak voltage amplitude, f is the driving frequency, Φ_{signal} is the signal's phase and V_{offset} is the signal's offset voltage. Typical operation of the the actuator requires $A_{peak-to-peak}$ in the order of 200 V to 300 V [1].

The prototype was mounted onto a laser cut acrylic base and was filmed by a high speed camera with fiber optic light sources illuminating the device. For the first test, we drove the control actuator at 1 Hz with $A_{peak-to-peak}$ set to 280V (see supplemental video). $\psi_{0J,i}$ was measured by post-processing the video frames (Fig. 8). Then, the displacement of the control actuator tip was measured by manually tracking its midpoint. Next, a sinusoidal fit to the data (Fig. 7) was applied. With $\delta_{C_{I_y}}$ extracted from the experimental data, we simulated the RoboBee to compare how the physical prototype performed relative to the kinematic model.

[1] Although the input voltages are high, current draw is in the order of 1 mA [19]

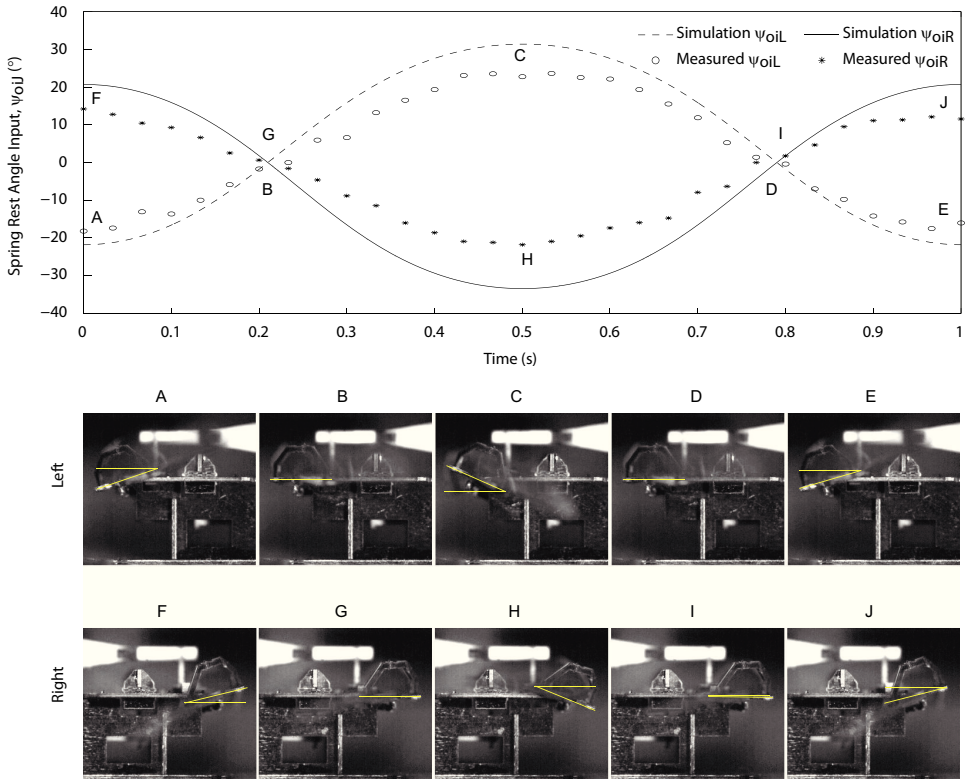

Fig. 8. The control actuator is driven at 1 Hz which causes the left and right wing to rotate differentially. Here, we compare the wing spring rest angle input $\psi_{0J,i}$ of the left and right Sreetharan linkages to the prediction from the kinematic model.

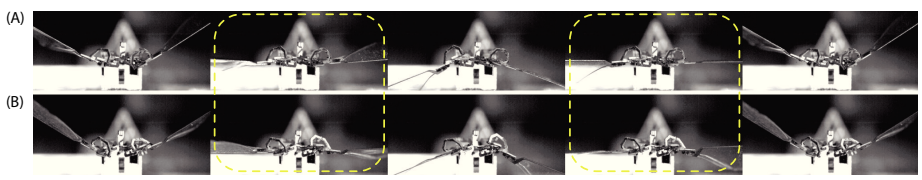

Fig. 9. Power actuator frequency at 80 Hz. (A)The control actuator with a V_{offset} of 10V is deflected in the $-\hat{n}_y$ direction. (B) The control actuator with a V_{offset} of 290V is deflected in the $\hat{n}_y$ direction. Highlighted are the mid-strokes of both cases showing the difference in the AoA during the upstroke and downstroke (time between frames is ≈ 3.2 ms).

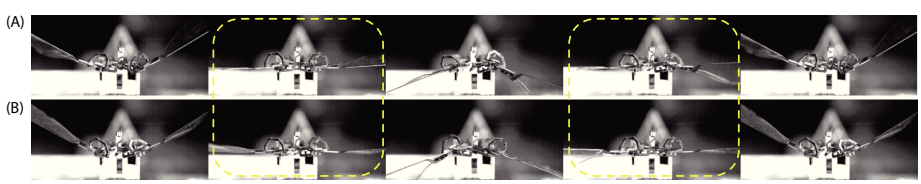

Fig. 10. Power and Control actuators were driven at 80 Hz. (A) Control actuator moving in anti-phase with mid-stroke wing velocity. (B) Control actuator moving in phase with mid-stroke wing velocity. Highlighted are the mid-strokes of both cases showing the difference in the AoA during the upstroke and downstroke (time between frames is ≈ 3.2 ms).

As seen in Fig. 8, the kinematic model consistently over predicts the wing hinge spring rest angle by as much as 35% on the right side and 29% on the left side. This could be due to a number of reasons. The main source of error likely stems from the assembly of the spherical four-bar linkage and the Sreetharan linkage. These two components are made in a planar 2D scaffold and then manually folded with the aid of kinematic stops. This method, though easy to implement, is unable to make precise 90° folds. The second source of error arises from the narrow joints in the spherical linkages. Most of the joint widths are around 300 μm. The narrower the joint, width wise (joint geometry is defined in [16]), its behavior starts to deviate further from an ideal revolute joint due to the off-axis compliance of the flexure, and becomes more like a ball and socket joint. Such errors would cause this prototype to have kinematics that deviate from the model.

The next set of tests involved driving the power and

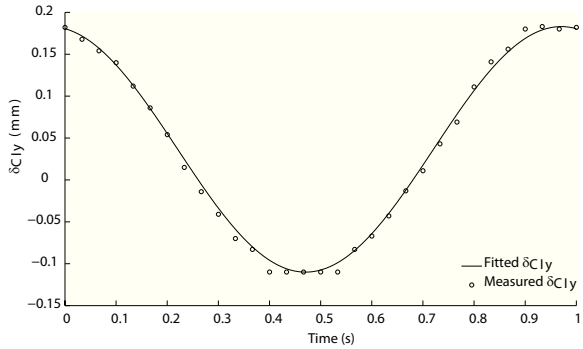

Fig. 7. Measurement of the control actuator tip deflection. A sinusoidal fit to the measurements was made to be fed back into the simulation to compare the kinematic model with the prototype.

control actuator at the system's resonant frequency (which was empirically found to be 80 Hz) to see if we can generate wing motions that could potentially produce yaw and roll torques as highlighted in section III(see supplemental video). For yaw, we drove the power actuator at 80 Hz with $A_{peak-to-peak}$ set to 260V and the control actuator at a $A_{peak-to-peak}$ set to 0V, f at 0 Hz and V_{offset} set to 10V followed by 290V. Images retrieved from the high speed camera (images were captured at 5000 fps) qualitatively confirmed that the mechanism produced wing motions that in simulation could generate 0.14 μNm of yaw torque (Fig. 4(A), (B) and Fig. 9). In a like manner, wing motions to generate potential roll torques were created by driving the power and control actuator at 80 Hz. In-phase motions of the control actuator tip with $\dot{\phi}_J$ was achieved by introducing a phase difference of $90°$ between the power actuator and control actuator while anti-phase motions were made by driving the control actuator with a phase of -$90°$ with respect to the power actuator. Again, post-processing of images from the high speed video indicated that wing motions generated by such inputs from the power and control actuator could generate in simulation 1.34 μNm of roll torque (Fig. 4(C), (D) and Fig. 10).

V. Conclusion and Future Work

We showed in this work that the Sreetharan linkage in combination with a spherical four-bar linkage can effectively decouple the power input and control input to the RoboBee's wings. By using a single control actuator, as opposed to two [9], considerable weight savings can be made. In order to use a single control actuator and a single power actuator, an innovative combination of two spherical four-bar linkages, two Sreetharan Linkages and four planar four-bar linkages was developed. Although there are differences between the experimental performance and the kinematic model, the prototype demonstrated its ability to cause differential AoA with trends consistent with the kinematics. Fruit fly data [12], indicates that a $\triangle\psi_0$ of $\approx 15°$ is sufficient to enable turning maneuvers. Encouragingly, this RoboBee could generate a peak-to-peak $\triangle\psi_0$ of $\approx 45°$ (Fig. 8).

Although the simulated torques (as inferred from wing kinematics) are lower than measured roll and yaw torques generated by Finio's [9] and Ma's [10] designs, we expect that torque generation capability of this concept will improve by using a more precise fabrication technique [17].

In the future, roll and yaw torques generated by differential AoA will have to be measured to verify the feasibility of such a control scheme. Only then will a flight weight version be built through optimization of the control actuator size, strategic placement of the passive wing hinge (to minimize the aerodynamic load on the control actuator) and tuning of the wing hinge stiffness.

References

[1] M. Keennon, K. Klingebiel, H. Won, and A. Andriukov, "Development of the nano hummingbird: A tailless flapping wing micro air vehicle," in *AIAA Aerospace Sciences Meeting*, 2012.

[2] I. Kroo and P. Kunz, "Development of the mesicopter: A miniature autonomous rotorcraft," in *American Helicopter Society (AHS) Vertical Lift Aircraft Design Conference, San Francisco, CA*, 2000.

[3] H. Tanaka, K. Hoshino, K. Matsumoto, and I. Shimoyama, "Flight dynamics of a butterfly-type ornithopter," in *Intelligent Robots and Systems, 2005. (IROS 2005). 2005 IEEE/RSJ International Conference on*, aug. 2005, pp. 2706 – 2711.

[4] E. Ulrich, D. Pines, and J. Humbert, "From falling to flying: the path to powered flight of a robotic samara nano air vehicle," *Bioinspiration & Biomimetics*, vol. 5, p. 045009, 2010.

[5] W. S. N. Trimmer, "Microbots and micromechanical systems," *Sensors and Actuators*, vol. 19, pp. 267–287, 1989.

[6] R. Dudley, *The biomechanics of insect flight: form, function, evolution*. Princeton Univ Pr, 2002.

[7] A. Bergou, S. Xu, and Z. Wang, "Passive wing pitch reversal in insect flight," *Journal of Fluid Mechanics*, vol. 591, pp. 321–338, 2007.

[8] R. J. Wood, "Liftoff of a 60mg flapping-wing mav," in *Proc. IEEE/RSJ Int. Conf. Intelligent Robots and Systems IROS 2007*, 2007, pp. 1889–1894.

[9] B. Finio and R. Wood, "Open-loop roll, pitch and yaw torques for a robotic bee," in *Intelligent Robots and Systems (IROS), 2012 IEEE/RSJ International Conference on*. IEEE, 2012.

[10] K. Ma, S. Felton, and R. Wood, "Design, fabrication, and modeling of the split actuator microrobotic bee," in *Intelligent Robots and Systems (IROS), 2012 IEEE/RSJ International Conference on*. IEEE, 2012.

[11] H. Mahjoubi and K. Byl, "Modeling synchronous muscle function in insect flight: a bio-inspired approach to force control in flapping-wing mavs," *Journal of Intelligent & Robotic Systems*, pp. 1–22, 2012.

[12] A. Bergou, L. Ristroph, J. Guckenheimer, I. Cohen, and Z. Wang, "Fruit flies modulate passive wing pitching to generate in-flight turns," *Physical review letters*, vol. 104, no. 14, p. 148101, 2010.

[13] R. J. Wood, "The first takeoff of a biologically inspired at-scale robotic insect," *IEEE Journal of Robotics and Automation*, vol. 24, no. 2, pp. 341–347, 2008.

[14] P. Mitiguy, *Advanced Dynamics and Motion Simulation*, 2010.

[15] P. Sreetharan and R. Wood, "Mechanical intelligence in millimeter-scale machines," *Harvard University, School of Engineering and Applied Science*.

[16] J. Whitney and R. Wood, "Aeromechanics of passive rotation in flapping flight," *Journal of Fluid Mechanics*, vol. 660, no. 1, pp. 197–220, 2010.

[17] P. Sreetharan, J. Whitney, and R. Strauss M, and Wood, "Monolithic fabrication of millimeter-scale machines," *Journal of Micromechanics and Microengineering*, 2012.

[18] R. Wood, E. Steltz, and R. Fearing, "Optimal energy density piezoelectric bending actuators," *Sensors and Actuators A: Physical*, vol. 119, no. 2, pp. 476–488, 2005.

[19] M. Karpelson, G.-Y. Wei, and R. J. Wood, "Driving high voltage piezoelectric actuators in microrobotic applications," *Sensors and Actuators A: Physical*, vol. 176, no. 0, pp. 78 – 89, 2012. [Online]. Available: http://www.sciencedirect.com/science/article/pii/S0924424711006947